



HAL
open science

Cs(2)Ln(3)CuS(8) (Ln = La-Nd, Sm-Tb): Synthesis, Crystal Structure, and Magnetic and Optical Properties

Tatiana A. Pomelova, Charlene Delacotte, Natalia V. Kuratieva, Pierric Lemoine, Stéphane Cordier, Sangjun Park, Thierry Guizouarn, Vincent Pelletier, Régis Gautier, Nikolay G. Naumov

► To cite this version:

Tatiana A. Pomelova, Charlene Delacotte, Natalia V. Kuratieva, Pierric Lemoine, Stéphane Cordier, et al.. Cs(2)Ln(3)CuS(8) (Ln = La-Nd, Sm-Tb): Synthesis, Crystal Structure, and Magnetic and Optical Properties. *Inorganic Chemistry*, 2023, 62 (17), pp.6586-6597. 10.1021/acs.inorgchem.2c03447 . hal-04088900

HAL Id: hal-04088900

<https://hal.science/hal-04088900v1>

Submitted on 24 May 2023

HAL is a multi-disciplinary open access archive for the deposit and dissemination of scientific research documents, whether they are published or not. The documents may come from teaching and research institutions in France or abroad, or from public or private research centers.

L'archive ouverte pluridisciplinaire **HAL**, est destinée au dépôt et à la diffusion de documents scientifiques de niveau recherche, publiés ou non, émanant des établissements d'enseignement et de recherche français ou étrangers, des laboratoires publics ou privés.

$\text{Cs}_2\text{Ln}_3\text{CuS}_8$ (Ln = La-Nd, Sm-Tb): Synthesis, crystal structure, magnetic and optical properties.

Tatiana A. Pomelova^a, Charlène Delacotte^b, Natalia V. Kuratieva^a, Pierrick Lemoine^{b†}, Stéphane Cordier^b, SangJun Park^c, Thierry Guizouarn^b, Vincent Pelletier^b, Regis Gautier^b, Nikolay G. Naumov^{a}*

^aNikolaev Institute of Inorganic Chemistry SB RAS, 3, Akad. Lavrentiev Ave., 630090
Novosibirsk, Russian Federation

^bUniv Rennes, Ecole Nationale Supérieure de Chimie de Rennes, CNRS, ISCR–UMR 6226, F-
35000, Rennes, France.

^cNovosibirsk State University, 2, Pirogova Str., 630090 Novosibirsk, Russian Federation

KEYWORDS lanthanide sulfide, crystal structure, magnetic properties, magnetocaloric, DFT calculations.

ABSTRACT This work reports the preparation of the new quaternary sulfides $\text{Cs}_2\text{Ln}_3\text{CuS}_8$ (Ln = La-Nd, Sm-Tb), their original crystal and electronic structures and their magnetic properties. The sulfides were prepared using reactive flux method from mixtures of Ln_2S_3 (EuS), Cs_2S_6 , Cu_2S and S. They crystallize in a new type of structure ($C2/m$ space group) and exhibit a layered-like crystal structure which is hybrid of those of the ACe_2CuS_6 series (A = Cs and K) and that of $\text{K}_2\text{CeCu}_2\text{S}_4$.

The values of the optical band gap calculated by the Kubelka-Munk equation are in range of 1.2 – 2.62 eV depending of the nature of Ln ion. The Cs₂Gd₃CuS₈ compound displays relatively great magnetic refrigerating properties at cryogenic temperature with a mass entropy change ($-\Delta S_M$) reaching 19.5 J kg⁻¹ K⁻¹ at 3.5K for $\Delta H = 5$ T.

Introduction

Rare-earth based chalcogenides containing transition metal are considered as promising functional materials due to their unique structural diversity and their thermal, electrical, magnetic and optical properties. For example, ALnMQ₃ compounds (A=Rb, Cs; Ln=rare-earth; M=Mn, Co, Zn, Cd, Hg; Q = S, Se, Te) are semiconductors demonstrating magnetic properties with an optical band gap value depending of chemical composition and crystal orientation,^{1, 2} A_xLn₂Cu_{6-x}Te₆ (A=K-Cs; Ln=La-Nd 0.65<x<0.77) show thermoelectric properties,³⁻⁵ and ALnMTe₄ (A=K, Na; M=Cu, Ag; Ln=La, Ce) exhibits charge density waves.⁶

A huge number of alkali-metal/rare-earth/transition-metal/chalcogenides (A/Ln/M/Q) synthesized by reactive-flux technique⁷ have been discovered over the past decades.^{1, 2, 8, 9} The low melting points of the A_xQ_y fluxes (433-723 K) and their ability to act as both reagent and reaction medium led to the characterization of kinetically stabilized species that cannot be obtained by the use of traditional high-temperature experimental methods. Most of these chalcogenide compounds are characterized by layered-like (anionic layers + alkali metal cations between them) or tunnel structures.⁸

The quaternary A-M-Ln-S system with M = copper was one of those investigated first. Several copper-based systems are reported in literature: ALn₂CuS₆ family,¹⁰⁻¹³ K₂CeCu₂S₄,¹⁰ CsCeCuS₃¹¹ with a layered-like structure and ALn₂CuS₄, A₂Ln₄Cu₄S₉,⁹ as well as CsLn₂Cu₃S₅¹⁴ which crystal structures contain tunnels. All known compounds, to the best of our knowledge, are

summarized in Table 1. The investigation of the Cs-Ln-Cu-S systems has allowed us to discover the new series of title compounds $\text{Cs}_2\text{Ln}_3\text{CuS}_8$, which exhibit a new layered-like structure type being hybrid structure of that of the ALn_2CuS_6 ¹¹ series and $\text{K}_2\text{CeCu}_2\text{S}_4$.¹⁰ As one can see in Table 1, the small Ln^{3+} cations (Gd- Er) tend to favor the formation of tunnel structures, whereas the big ones favor the formation of layered-like structures. From the crystal chemistry point of view, this new $\text{Cs}_2\text{Ln}_3\text{CuS}_8$ structural type is of prime interest as the number of members of this series (Ln=La, Ce, Pr, Nd, Sm, Eu, Gd, and Tb) is the largest one among all the other related series based on different-sized Ln^{3+} cations. In this article we report the syntheses, structural features, optical and magnetic properties of this new $\text{Cs}_2\text{Ln}_3\text{CuS}_8$ family for which all members crystallize in the same structure-type with Ln=La, Ce, Pr, Nd, Sm, Eu, Gd, and Tb.

Table 1. Formula and structure motif of compounds in the A-Ln-Cu-S systems

Series	Ref.	La	Ce	Pr	Nd	Sm	Eu	Gd	Tb	Dy	Ho	Er	Tm	Yb	Lu	
KLn_2CuS_6	10-13	Red														
$\text{K}_2\text{Ln}_2\text{CuS}_4$	10	Red														
CsLnCuS_3	11	Red														
$\text{CsLn}_2\text{CuS}_6$	11	Red														
$\text{Cs}_2\text{Ln}_3\text{CuS}_8$	This work	Blue														
KLn_2CuS_4	9				Grey			Grey		Grey						
$\text{K}_2\text{Ln}_4\text{Cu}_4\text{S}_9$	9				Grey			Grey		Grey						
$\text{RbLn}_2\text{CuS}_4$	15				Grey			Grey								
$\text{RbLn}_2\text{Cu}_3\text{S}_5$	15				Grey						Grey					
$\text{Rb}_2\text{Ln}_4\text{Cu}_4\text{S}_9$	15				Grey			Grey								
$\text{CsLn}_2\text{Cu}_3\text{S}_5$	15				Grey					Grey						
$\text{Cs}_2\text{Ln}_4\text{Cu}_4\text{S}_9$	14				Grey					Grey		Grey				

Red- layered-like crystal structure, grey – tunnel crystal structure, blue – present work materials.

Experimental methods

Synthesis

Cs₂S_x. A starting mixture of alkali metal polysulfides was prepared by a similar method as that reported for K₂S_x¹³ from Cs₂CO₃ (high purity) and NH₄SCN vapor as the sulfurization agent. We repeated the sulfurization process at 573 K, and we performed a chemical test with a BaCl₂ containing water solution after each iteration for the determination of the moment when all carbonate groups are replaced by polysulfide ones. A red-orange hygroscopic powdered mixture consisting of Cs₂S_x (x = 3–6, main fraction is Cs₂S₆) according to powder X-ray diffraction (PXRD) was obtained.

Cs₂Ln₃CuS₈. 0.6 mmol of Ln₂S₃ (0.3 mmol EuS) and 0.2 mmol of Cu₂S (0.1 mmol of Cu₂S in case of Ln=Eu) were ground together in an agate mortar and then placed in a glass ampule with 2 mmol of S and 0.8 mmol of Cs₂S₆. The ampule was then evacuated to roughly 5×10^{-2} Torr, sealed, and placed in a programmable furnace. The following temperature profile was used: heating with a rate of 2 K/min to 673 K, temperature plateau for 120 h, cooling to 423 K with a rate of 10 K/h, and then quenching at 323 K. The orange-yellow (Ln=La, Nd, Sm, Gd, Tb), yellow-green (Ln=Pr), black (Ln=Eu) or dark red-brown (Ln=Ce) powders were obtained by washing the crude product with distilled water and drying in a vacuum. The yields based on Ln were 95-98%. The purity of products was confirmed by PXRD. To grow single crystals suitable for crystal structure determination, a large excess of S and Cs₂S_x (5–8 mol to 1 mol of Ln₂S₃) was used.

Characterization Techniques

The PXRD data collections were performed on a Philips PW1820/1710 diffractometer with Philips PW1711/10 Proportional Detector (CuK α radiation, graphite monochromator, $2\theta = 5^\circ$ – 70° , measurement time 4sec/point, increment size 0.05°). Rietveld analysis including preferred orientation simulation was carried out using GSAS-II software.¹⁶

X-ray diffraction data were collected from needle-shaped single-crystals using graphite monochromatized MoK α -radiation ($\lambda = 0.71073 \text{ \AA}$) at 293(2) K on a Bruker APEX DUO diffractometer equipped with a 4K CCD area detector. The color of single-crystals was yellow for Ln=La, Pr, Nd, Sm, Gd, Tb) and black for Ln=Eu. The ϕ - and ω -scan technique was employed to measure the intensities. Absorption corrections were applied empirically using the SADABS program.¹⁷ Structures were solved by the direct methods and further refined by the full-matrix least-squares method using the SHELXTL package.¹⁸

The diffuse reflectance spectrum of powdered bulk samples was recorded with a UV-3101 PC Shimadzu spectrometer equipped with integrating sphere and BaSO₄ as reference in the range of 200–800 nm. The Kubelka–Munk function was used to convert diffuse reflectance data to absorption spectra.

Magnetic and magnetocaloric measurements were performed using a SQUID magnetometer (MPMS XL5, Quantum Design). Zero field cooled (ZFC) measurement was carried out from 1.8 to 300 K at a constant applied magnetic field of 0.1 T. The molar magnetic susceptibilities were corrected from the intrinsic diamagnetism evaluated from Pascal's tables :

$\chi_{D_{Cs^+}} = -35 \times 10^{-6} \text{ cm}^3 \text{ mol}^{-1}$, $\chi_{D_{Ce^{3+}}} = \chi_{D_{Pr^{3+}}} = \chi_{D_{Nd^{3+}}} = \chi_{D_{Eu^{3+}}} = \chi_{D_{Gd^{3+}}} = -20 \times 10^{-6} \text{ cm}^3 \text{ mol}^{-1}$, $\chi_{D_{Tb^{3+}}} = -19 \times 10^{-6} \text{ cm}^3 \text{ mol}^{-1}$, $\chi_{D_{Cu^+}} = -12 \times 10^{-6} \text{ cm}^3 \text{ mol}^{-1}$ and $\chi_{D_{S_2^{2-}}} = -30 \times 10^{-6} \text{ cm}^3 \text{ mol}^{-1}$.¹⁹ Note that the chemical bonding encountered in the (S₂)²⁻ dimers as well as the presence of Eu²⁺ in Cs₂Eu₃CuS₈ was not considered in the diamagnetism susceptibility correction. Hence, the applied diamagnetic susceptibility corrections were $-382 \times 10^{-6} \text{ cm}^3 \text{ mol}^{-1}$ for Cs₂Ln₃CuS₈ (Ln = Ce, Pr, Nd, Eu, Gd) and $-379 \times 10^{-6} \text{ cm}^3 \text{ mol}^{-1}$ for Cs₂Tb₃CuS₈. The magnetocaloric properties were determined from magnetic entropy change, ΔS_M , evaluated using one of the Maxwell relations:

$$\Delta S_M(T)_{\Delta H} = \mu_0 \int_0^{H_f} \left(\frac{\partial M(T, H)}{\partial T} \right)_H dH \quad (1)$$

The numerical integration of Eq. (1) was carried out using the method proposed by Pecharsky and Gschneidner Jr.²⁰, from magnetization isotherms recorded on heating from 2 K to 26 K in applied magnetic fields up to 5 T, with field steps of 0.2 T and temperature increments of 1 K.

Computational details

Spin-polarized band structure and average properties of were computed with the DFT Vienna ab initio Simulations Package (VASP).²¹ The exchange–correlation energy was taken into account using the generalized gradient approximation (GGA) with the Perdew–Burke–Ernzerhof (PBE) functional.²² The energy cutoff in the calculations is 400 eV. The electronic wave function was sampled with $4 \times 4 \times 4$ k-points in the first Brillouin zone using the Monkhorst-Pack method.²³ Chemical bonding analyses of plane-wave data by Crystal Orbital Hamiltonian Population (COHP)²⁴ were done using LOBSTER.^{25–27} Band-structures, density of states (DOS) and COHP curves were shifted so that the Fermi level lies at 0 eV.

Results and discussion

Synthesis

Eight new quaternary chalcogenides with general formula $\text{Cs}_2\text{Ln}_3\text{CuS}_8$ (Ln=La, Ce, Pr, Nd, Sm, Eu, Gd, and Tb) were synthesized using the conventional reactive flux method. The reaction of Ln_2S_3 (or EuS) and Cu_2S in melted Cs_2S_x results in powder product along with few single-crystals in the shape of needles and plates. Unfortunately, we weren't able to grow $\text{Cs}_2\text{Ce}_3\text{CuS}_8$ single-crystal suitable for a crystal structure determination. However, the x-ray powder diffraction pattern of $\text{Cs}_2\text{Ce}_3\text{CuS}_8$ demonstrated strong similarities with those of the other members of $\text{Cs}_2\text{Ln}_3\text{CuS}_8$ family in agreement with the stabilization of a unique structure-type. Concerning the syntheses conditions for Ln=Ce a greater excess of Cs_2S_x (molar ratio up to 4Cs:1Ln, at least 8Cs:3Ln) is

needed to prevent formation of the $\text{CsCe}_2\text{CuS}_6$ as secondary phase. We failed to prepare phase pure $\text{Cs}_2\text{La}_3\text{CuS}_8$ sample under the applied synthesis conditions, it always contained $\text{CsLa}_2\text{CuS}_6$ (isostructural to $\text{CsCe}_2\text{CuS}_6^{11}$) phase as by-product. Note that admixture of hypothetical $\text{CsLn}_2\text{CuS}_6$ phase was also found for some experiments with Pr, Nd, Sm, and Gd. Thus, for $\text{Ln}=\text{Ce-Sm}$, the molar ratio of Ln_2S_3 to Cu_2S seems to determine the product of the reaction. No traces of $\text{CsLn}_2\text{CuS}_6$ phase were found for Eu and Tb samples. In a case of $\text{Ln}=\text{Tb}$, for initial loading ratio of $\text{Tb}_2\text{S}_3:\text{Cu}_2\text{S} = 1:2$ a phase isostructural to $\text{CsDy}_2\text{Cu}_3\text{S}_5^{14}$ starts to produce as a resulting product. However, the lack of single crystals prevented further investigation on these samples.

It could be noted, that using stoichiometric amount of Cs_2S_6 ($\text{Ln}_2\text{S}_3:\text{Cs}_2\text{S}_6 = 3:2$, $\text{Ln}=\text{La-Nd, Sm}$) in the synthesis leads to mixture of $\text{CsLn}_2\text{CuS}_6$ and $\text{Cs}_2\text{Ln}_3\text{CuS}_8$ phases despite the initial loading of other sulfides. On other hand, for $\text{Ln}=\text{Gd, Eu}$ the $\text{Cs}_2\text{Ln}_3\text{CuS}_8$ phase seems to be preferentially formed in all tested synthesis conditions. All experimental details as well as obtained products are shown in Table 2.

Table 2. Ratio of components and main products in $\text{Cs}_2\text{Ln}_3\text{CuS}_8$ synthesis.

Cs-Ln-Cu-S	La	Ce	Nd-Sm	Eu	Gd	Tb
$2\text{Ln}_2\text{S}_3+\text{Cu}_2\text{S}+4\text{Cs}_2\text{S}_6$	$\text{CsLn}_2\text{CuS}_6$		$\text{Cs}_2\text{Ln}_3\text{CuS}_8$		$\text{CsTb}_2\text{Cu}_3\text{S}_5(?)$	
$3\text{Ln}_2\text{S}_3+\text{Cu}_2\text{S}+4\text{Cs}_2\text{S}_6$	$\text{CsLn}_2\text{CuS}_6+$ $\text{Cs}_2\text{Ln}_3\text{CuS}_8$		$\text{Cs}_2\text{Ln}_3\text{CuS}_8$			
$3\text{Ln}_2\text{S}_3+\text{Cu}_2\text{S}+8\text{Cs}_2\text{S}_6$	$\text{CsLn}_2\text{CuS}_6+$ $\text{Cs}_2\text{Ln}_3\text{CuS}_8$	$\text{Cs}_2\text{Ln}_3\text{CuS}_8$				
$2\text{Ln}_2\text{S}_3+\text{Cu}_2\text{S}+2\text{Cs}_2\text{S}_6$	$\text{CsLn}_2\text{CuS}_6+$		$\text{Cs}_2\text{Eu}_3\text{CuS}_8$		$\text{Cs}_2\text{Gd}_3\text{CuS}_8$ $+\text{CsGd}_2\text{CuS}_6$ (traces)	No reaction
$3\text{Ln}_2\text{S}_3+\text{Cu}_2\text{S}+2\text{Cs}_2\text{S}_6$	$\text{Cs}_2\text{Ln}_3\text{CuS}_8$					

Crystal structure

All crystallographic data and selected calculated bond lengths are summarized in Table 3 and Table S2-S3, respectively. The eight members of the $\text{Cs}_2\text{Ln}_3\text{CuS}_8$ series all crystallize in the monoclinic space group $\text{C2}/m$ ($\text{N}^\circ 12$). There are two crystallographically independent Ln positions, one Cu and four S positions in the anionic layer $\{\text{Ln}_3\text{CuS}_8\}$ and one Cs position between these layers. All atoms are located on $4i$ Wyckoff positions, excepted Ln1 which is located in $2c$ position. Ln1 is coordinated to six S^{2-} anions forming a distorted octahedron noted $\{\text{Ln1S}_6\}$ with two opposite short Ln-S bonds and four long ones. Ln2 has a bicapped trigonal prism coordination noted $\{\text{Ln2S}_4(\text{S}_2)_2\}$. It is built up from four S^{2-} (apex and capped positions in prisms) and two $(\text{S}_2)^{2-}$ groups forming edges of the prisms (Figure 1A). The S-S interatomic distances within the dimers roughly equal to 2.08 Å. This value is close to ones reported for ALn_2CuS_6 series¹⁰⁻¹³ or CuS_2 ²⁸ Each prism is connected with two neighboring ones by shared triangular faces, forming chains $\{\text{Ln2S}_4(\text{S}_2)_2\}$ in a pattern similar to those observed in the $\text{CsCe}_2\text{CuS}_6$ crystal structure type.¹⁰ Two of the latter chains of $\{\text{Ln2S}_4(\text{S}_2)_2\}$ are connected together via shared capping edges of the prisms. Considering one $\{\text{Ln2S}_4(\text{S}_2)_2\}$ prism involved in the connection of the chains, each opposite capping edge is shared with two edges of two $\{\text{Ln1S}_6\}$ octahedra. This second type of capping edge of $\{\text{Ln2S}_4(\text{S}_2)_2\}$ shared with $\{\text{Ln1S}_6\}$ octahedron is longer than the first type of capping edge shared between two $\{\text{Ln2S}_4(\text{S}_2)_2\}$ prisms described above. At the end, second type of chain is formed by the sharing of common edges between $\{\text{Ln1S}_6\}$ octahedra. The singularity of this structure is that it is based on two types of chains of rare earth atoms generated by the two types of coordination polyhedrons, the $\{\text{Ln2S}_4(\text{S}_2)_2\}$ prisms and the $\{\text{Ln1S}_6\}$ octahedrons, and their interconnections modes. Several magnetic interactions are thus expected: within each of the two types of chains and between the chains. The Cu atoms lie in tetrahedral voids located between prisms and octahedron (Figure S1 in SI), formed by two edges of two adjacent $\{\text{Ln1S}_6\}$ octahedra

and two cape edges of two neighboring $\{\text{Ln}_2\text{S}_4(\text{S}_2)_2\}$ prisms. The occupancy of Cu positions was found to be 50% except for Eu. In the case of Eu, the refinement of the Cu position occupancy deviates from 50% within the estimated standard deviations. The consequence on the oxidation state of Eu will be discussed below. The alternation of $\{\text{Ln}_2\text{S}_4(\text{S}_2)_2\}$ - $\{\text{Ln}_2\text{S}_4(\text{S}_2)_2\}$ and $\{\text{Ln}_1\text{S}_6\}$ fragments (Figure 1B) lead to distorted $\{\text{Ln}_1(\text{Ln}_2)_2\text{CuS}_8\}^{2-}$ of anionic layers staked along c-axis. The Cs cations are located between the layers in a wavy disposition (Figure 1C). Crystallographic environment of Cs atom could be described as distorted rectangular prism with one cap leading to a coordination number of 9 (Figure S1C in SI).

Table 3. Structure data and refined parameters for $\text{Cs}_2\text{Ln}_3\text{CuS}_8$ (Ln = La-Nd, Sm-Tb)

Ln	La	Ce*	Pr	Nd	Sm	Eu	Gd	Tb
Crystal system	monoclinic							
Space group	<i>C2/m(No12)</i>							
a, Å	16.904(2)	16.78	16.709(3)	16.678(2)	16.535 (1)	16.4383(8)	16.443(1)	16.352(2)
b, Å	4.2482(4)	4.203	4.1811(5)	4.1578(6)	4.1110(2)	4.1047(2)	4.0703(2)	4.0451(4)
c, Å	11.997 (1)	11.97	11.9516(19)	11.9499(17)	11.9041(8)	11.9340(6)	11.8808(7)	11.8505(12)
β, deg	115.209(4)	115.41	115.228(5)	115.201(3)	115.177(2)	114.582(4)	115.098(2)	115.183(3)
V, Å ³	779.48	762.84	755.32	749.78	732.34	732.26	720.09	709.39
Z	2							
ρ _{calc} , g/cm ³	4.272	4.33	4.435	4.512	4.702	5.013	4.878	4.975
μ, mm ⁻¹	15.035	-	16.707	17.471	19.280	21.516	21.191	22.441
crystal size, mm ³	0.100 x 0.020 x 0.005	-	0.180 x 0.030 x 0.010	0.190 x 0.030 x 0.005	0.200 x 0.020 x 0.020	0.110 x 0.020 x 0.005	0.100 x 0.020 x 0.010	0.100 x 0.005 x 0.002
θ range, deg.	2.521 - 28.272	-	1.884 - 28.312	1.883 -30.709	1.890 - 30.742	2.587 -27.507	1.893 -30.622	2.595 -27.484
R1 (wR2) for I ≥ 2σ(I)	0.0447(0.0933)	-	0.0515 (0.0903)	0.0176 (0.0395)	0.0154 (0.0365)	0.0369 (0.0932)	0.0228 (0.0399)	0.0386 (0.0691)
R1 (wR2)	0.0726 (0.0996)	-	0.0774 (0.0969)	0.0217 (0.0404)	0.0170 (0.0370)	0.0432 (0.0953)	0.0307 (0.0411)	0.0663 (0.0746)

*Structural data based on PXRD refinement (figure S2 in SI)

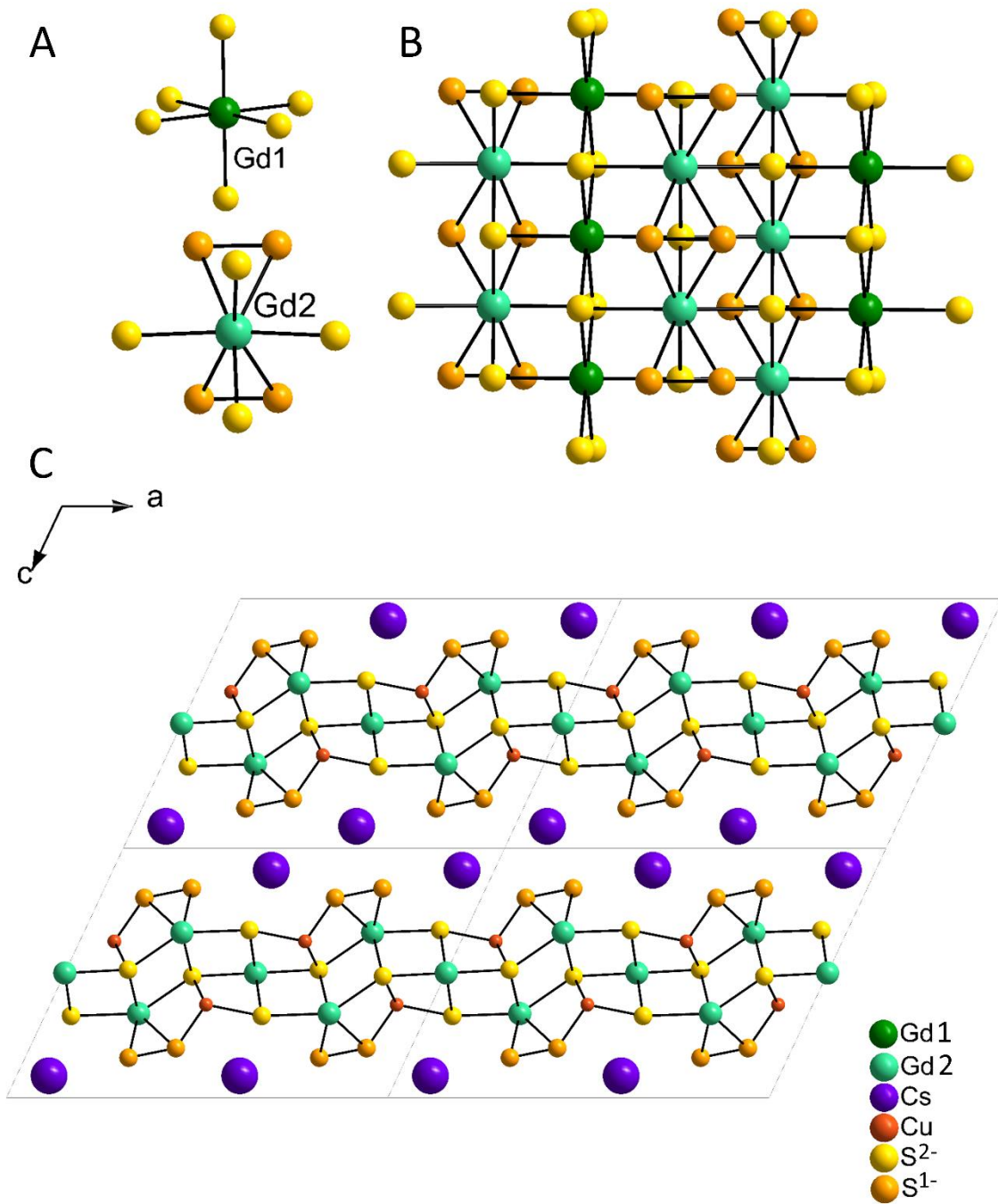


Figure 1. Crystallographic environment of Ln³⁺ cations (A), {Ln₂S₄(S₂)₂}·{Ln₂S₄(S₂)₂}·{LnS₆} part of anionic layer (B) and crystal structure of Cs₂Ln₃CuS₈ compounds (C).

The $\text{Cs}_2\text{Ln}_3\text{CuS}_8$ crystal structure is a combination between structures of the ALn_2CuS_6 family ($\text{A}=\text{K}$, Cs , $\text{Ln} = \text{La-Nd}$, Sm , Eu) and that of K_2CeCuS_4 (Figure 2). $\text{CsCe}_2\text{CuS}_6$ and KCuLn_2S_6 are characterized by layered-like structures crystallizing either in the space groups $C2/c$ ($\text{Ln} = \text{La-Nd}$, $\text{A} = \text{K}$), $Fddd$ ($\text{Ln} = \text{Sm}$, Eu , $\text{A}=\text{K}$) or $Immm$ ($\text{CsCe}_2\text{CuS}_6$). The structure of the ALn_2CuS_6 compounds is based on $\{\text{LnS}_4(\text{S}_2)_2\}$ bicapped trigonal prism similar to that described above for the title compounds. The triangular face of the prism is built up from one $(\text{S}_2)^{2-}$ dimer and one S^{2-} . The connection of the prisms by the triangular faces leads to infinite chains of lanthanide atoms. The chains are linked one to another by sharing S^{2-} atoms of the triangular faces with capping sulfur atoms of two other $\{\text{LnS}_4(\text{S}_2)_2\}$ bicapped trigonal prisms of two adjacent chains. Cu^+ ions are surrounded by 5 $\{\text{LnS}_4(\text{S}_2)_2\}$ prisms and 2 $\text{A}(\text{S}_2)_8$ polyhedrons. They reinforce the cohesion of the structure to form $\{\text{CuLn}_2(\text{S}_2)_2\text{S}_2\}^-$ anionic layers. Chains of Cu^+ cations spread in parallel to Ln chains with Cu-Cu interatomic distances of 4.20 Å. Alkali metal atoms are located between the layers in distorted cube made of one end of 8 S_2 dimers whose one end lies at the corners of the cube. An important difference between the structures $\text{Cs}_3\text{Ln}_3\text{CuS}_8$ and those of the members of the KLn_2CuS_6 series is the refined value of the Cu^+ sites occupancy. The crystal structure of $\text{Cs}_2\text{Ln}_3\text{CuS}_8$ is based on one independent copper site, which occupancy is 50%. On other hand, the structures of the members of the KLn_2CuS_6 series are based on two independent positions for copper (denoted $\text{Cu}(1)$ and $\text{Cu}(2)$ for sake of clarity). Their occupancy depends on the size of the rare earth that also influence the space group of the structures. The $\text{Cu}(1)/\text{Cu}(2)$ occupancy ratio ranges from 15/85 for $\text{Ln}=\text{Ce-Nd}$ to 100/0 for $\text{Ln} = \text{Sm}$ and Eu . This change is accompanied by symmetry evolutions leading to space group change from $C2/c$ ($\text{Ln}=\text{Ce-Nd}$) to $Fddd$ ($\text{Ln} = \text{Sm}$ and Eu). It is worth noting that the structures of $\text{CsCe}_2\text{CuS}_6$ and that of KLa_2CuS_6 are in a between situation, with a $\text{Cu}1/\text{Cu}2$ ratio of 50/50 as found in $\text{Cs}_2\text{Ln}_3\text{CuS}_8$.

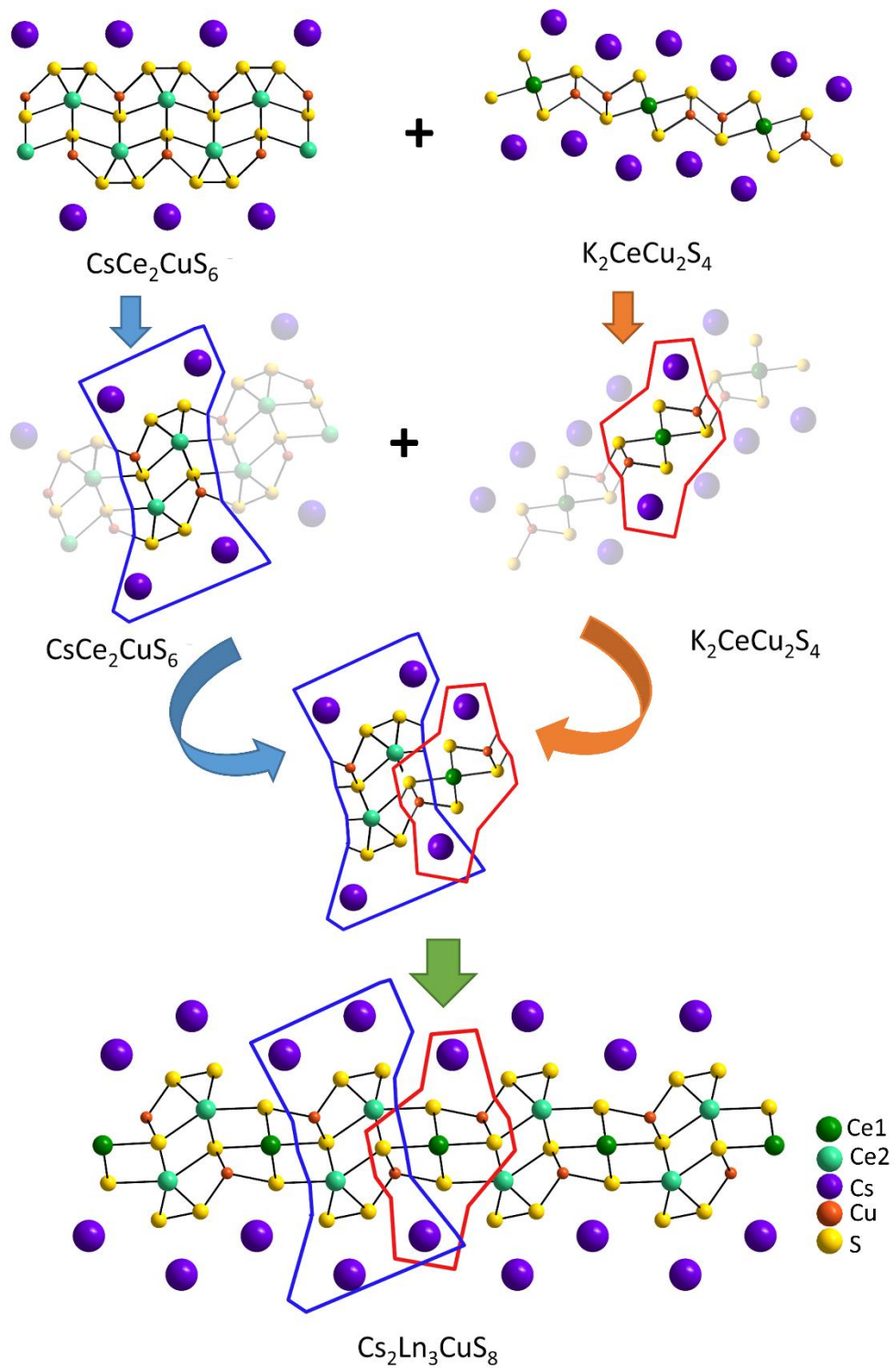


Figure 2. Correlations between $\text{Cs}_2\text{Ln}_3\text{CuS}_8$, $\text{CsCe}_2\text{CuS}_6$ and $\text{K}_2\text{CeCu}_2\text{S}_4$ crystal structures.

$\text{K}_2\text{CeCu}_2\text{S}_4$ is also characterized by a layered-like structure but that structure is based on $\{\text{CeS}_6\}$ octahedron and $\{\text{CuS}_4\}$ tetrahedron. The $\{\text{CeS}_6\}$ octahedra are connected through common edges leading to infinite chains of cerium atoms in one direction. The $\{\text{CuS}_4\}$ tetrahedra are also connected through common edges leading in that case to zig-zag chains of copper atoms in the same direction. These two kinds of chains are stacked in a second direction to form $\{\text{CeCu}_2\text{S}_4\}^{2-}$ anionic layers. Finally, potassium cations are located between the layers in a prism formed by seven sulfur atoms. This unusual coordination can be depicted considering a one corner truncated cube, leading to one square face and one triangular face in opposite position.

The correlation between the crystal structure of $\text{Cs}_2\text{Ln}_3\text{Cu}(\text{S}_2)_2\text{S}_4$ and those of ACe_2CuS_6 ($A = \text{K}$ and Cs) and $\text{K}_2\text{CeCu}_2\text{S}_4$ is also reflected through the tetrahedral coordination of copper atoms that can be viewed as ‘Janus ions’. Indeed, one side of the $\{\text{CuS}_4\}$ tetrahedron in $\text{Cs}_2\text{Ln}_3\text{Cu}(\text{S}_2)_2\text{S}_4$ is found in ACe_2CuS_6 whilst the other side corresponds to that found in $\text{K}_2\text{CeCu}_2\text{S}_4$ (Figure S4 in SI). The $\{\text{CuS}_4\}$ tetrahedron in $\text{Cs}_2\text{Ln}_3\text{Cu}(\text{S}_2)_2\text{S}_4$ shares three edges with three $\text{Ln}_2\text{S}_4(\text{S}_2)_2$ bicapped trigonal prisms, two edges with two $\{\text{LnS}_6\}$ octahedron and the last edge with one $\text{Cs}(\text{S}_2)_2(\text{S}_2)_{3/2}\text{S}_2$ prism. Hence, Cu^+ ions act as linkers between the Ln_1 chain and Ln_2 double chains to form $\{\text{Ln}_3\text{Cu}(\text{S}_2)_2\text{S}_4\}^{2-}$ anionic layers. As a consequence, the $\text{Cu}(\text{S}_2)_{1/2}\text{S}_3$ tetrahedron is strongly distorted with one short Cu-S (2.233-2.424 Å) bond involving one end of $(\text{S}_2)^{2-}$ dimer, and three longer Cu-S bonds (2.412-2.516 Å) involving discrete S^{2-} (Table S1 in SI). These bond values are correspond to those reported in $\text{CsCe}_2\text{Cu}(\text{S}_2)_2\text{S}_2$ (2.301 Å ($\times 2$) and 2.403 Å ($\times 2$) for Cu-S bonds involving one end of $(\text{S}_2)^{2-}$ dimers and discrete S^{2-} , respectively)¹¹ and in $\text{K}_2\text{CeCu}_2\text{S}_4$ (2.418 Å ($\times 2$) and 2.489 Å ($\times 2$)) for Cu-S bonds involving only discrete S^{2-} anions).¹⁰

It also should be noted, that the title $\text{Cs}_2\text{Ln}_3\text{CuS}_8$ compounds do not belong to any family of the numerous compounds reported in the literature and exhibiting the same stoichiometry

$A_2M^{2+}M_3^{4+}Q_8$ (A = alkali metals, Tl, Ag; Q = S, Se, Te, M^{2+} = Zn, Cd, Hg., M^{4+} = Sn, Ge.)^{29, 30, 31, 32}. Indeed, the latter compounds do not exhibit Q-Q bonds due to different metal charges, and their structures is a combination of tetrahedral and/or octahedral $\{M_3M'S_8\}$ frameworks. The only structural analogy that can be found with $Cs_2Ln_3CuS_8$ compounds concerns the layered-like nature of their structures.

As was mentioned above, two compounds among the series slightly differ from the others: $Cs_2Ce_3CuS_8$ and $Cs_2Eu_3CuS_8$. First, the colors of $Cs_2Ln_3CuS_8$ (Ln=La, Pr, Nd, Sm, Gd, and Tb) sulfides are different shades of yellow, while that of $Cs_2Ce_3CuS_8$ is dark red-brown and $Cs_2Eu_3CuS_8$ is black. If for Ce sulfides, such color seems common for other compounds (e.g. Ce_2S_3 is red, $CsCe_2CuS_6$ and KCe_2CuS_6 are red-brown, $CsCeCuS_3$ is black¹¹), the black color of europium compound suggests either non-stoichiometric chemical composition or the presence of Eu^{2+} cations along with Eu^{3+} . Crystal structure refinement of the Cu sites occupancies leads to the following chemical composition: $Cs_2Eu_3Cu_{1.46}S_8$. From this data, it appears that europium compound is a mixed valence system, suggesting that some Eu ions have a +2 charge. This is supported by the analysis of the averaged Ln-S bond lengths and unit cell volumes along the series (Figure 3 and Figure S5 in SI, respectively) evidencing longer Eu2-S bond lengths than those expected from a linear fit of all Ln1-S and Ln2-S bond lengths. From this analysis, it could be noted that Eu^{2+} cations should mostly occupy Ln2 position, in agreement with the fact, that bigger Eu^{2+} ions tend to occupy more loose position with complex environment and longer Eu-S bonds. This hypothesis about the mixed valence Eu^{2+}/Eu^{3+} is also confirmed by macroscopic magnetic measurements as discussed below.

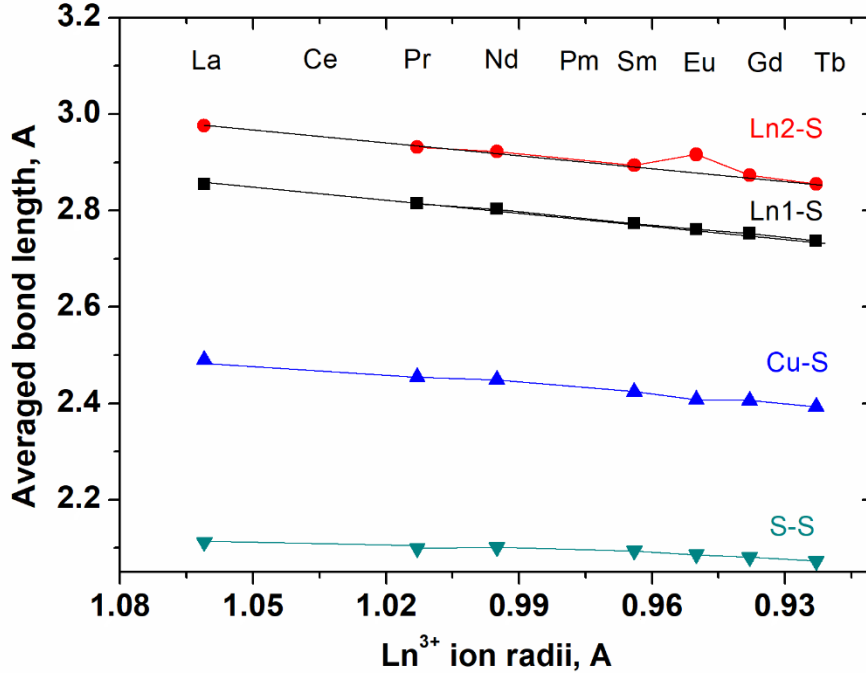


Figure 3. Averaged bond lengths for different $\text{Cs}_2\text{Ln}_3\text{CuS}_8$ compounds versus the Ln^{3+} ion radii.

Optical properties

The optical absorption spectra of $\text{Cs}_2\text{Ln}_3\text{CuS}_8$ were converted from the diffuse reflectance spectra using the Kubelka-Munk function. Band gaps were calculated as the intersection point between the photon energy axis and the line extrapolated from the linear portion of the absorption edge in a plot of Kubelka-Munk function. Resulting data are summarized in Table 4 and the optical absorption spectra are shown in Figure 4 and Figure S6 in SI. For $\text{Ln} = \text{Nd}$ and Pr additional peaks on the slope of the spectra were found. These peaks could be explained as $f-f$ (Nd) or $4f-5d$ (Pr)-transitions within the lanthanide ions.¹³ For Nd compound these transitions could be assigned to originate from the ground state $^4\text{I}_{9/2}$ to $^2\text{P}_{1/2}$ (~ 2.71 eV), $^2\text{G}_{9/2}$ (~ 2.48 eV) and $^2\text{G}_{7/2}$ (~ 2 eV)³³. Analysis of obtained E_g values revealed that the energy band gap increases as the ionic radii of Ln^{3+} increases. For Ce sulfide energy band gap was found to be much lower than ones for other

members of the $\text{Cs}_2\text{Ln}_3\text{CuS}_8$ family. The spectrum of $\text{Cs}_2\text{Eu}_3\text{Cu}_{1.46}\text{S}_8$ compound is difficult to interpret as it does not content absorption edge. However, due to the black color of the sample, its absorption edge is probably less than that of $\text{Cs}_2\text{Ce}_3\text{CuS}_8$. Calculated values are consistent with colors of the powders and suggested formula of $(\text{Cs}^+)_2(\text{Ln}^{3+})_3(\text{Cu}^+)(\text{S}_2^{2-})_2(\text{S}^{2-})_4$.

Table 4. Optical band gap of $\text{Cs}_2\text{Ln}_3\text{CuS}_8$ compounds

$\text{Cs}_2\text{Ln}_3\text{CuS}_8$	color	Band gap
<i>Ce</i>	red- brown	1.2 eV
<i>Pr</i>	yellow- green	2.37 eV
<i>Nd</i>	yellow- orange	2.42 eV
<i>Sm</i>	yellow- orange	2.48 eV
<i>Gd</i>	yellow- orange	2.56 eV
<i>Tb</i>	yellow	2.62 eV

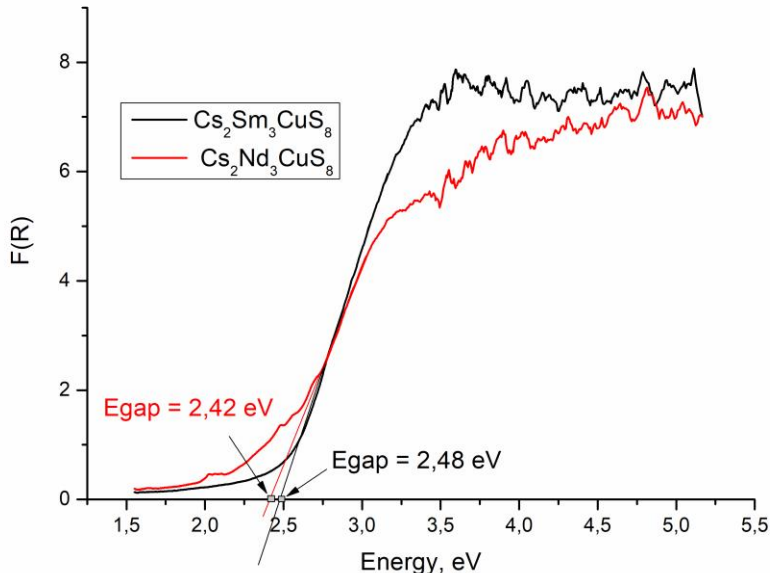


Figure 4. Optical absorption spectra of $\text{Cs}_2\text{Sm}_3\text{CuS}_8$ (black) and $\text{Cs}_2\text{Nd}_3\text{CuS}_8$ (red).

Magnetic properties

As previously mentioned, the chemical formula of the compounds can be written as $(\text{Cs}^+)_2(\text{Ln}^{3+})_3(\text{Cu}^+)_1(\text{S}_2^{2-})_2(\text{S}^{2-})_4$. Note that this assumption is incorrect for $\text{Cs}_2\text{Eu}_3\text{Cu}_{1.46}\text{S}_8$ as a mixed valence $\text{Eu}^{2+}/\text{Eu}^{3+}$ is strongly suggested. Nevertheless, as copper valence is +1, the only magnetic contribution comes from the rare-earth trivalent cations.

Among the $\text{Cs}_2\text{Ln}_3\text{CuS}_8$ series, compounds with $\text{Ln} = \text{Ce}, \text{Pr}, \text{Nd}, \text{Gd}$ and Tb exhibit classical magnetic behaviors, while the magnetic properties of Eu compound is more difficult to interpret due to the mixture of Eu^{2+} and Eu^{3+} cations (see below).

For the $\text{Cs}_2\text{Ce}_3\text{CuS}_8$, $\text{Cs}_2\text{Pr}_3\text{CuS}_8$, $\text{Cs}_2\text{Nd}_3\text{CuS}_8$, $\text{Cs}_2\text{Gd}_3\text{CuS}_8$ and $\text{Cs}_2\text{Tb}_3\text{CuS}_8$ compounds, the magnetic susceptibility curves do not evidence magnetic ordering on the investigated temperature range (1.8K-300K) as illustrated on Supporting Information Figures S7- S11, respectively. This indicates that the five compounds are Curie-paramagnets, which is supported by the magnetization data recorded at 2K (Figure S12). Indeed, the curves profiles are in agreement with a Brillouin

function as expected at low temperature for Curie-paramagnets. The inverse susceptibility data were analyzed using the Curie-Weiss law $\chi_M = C/(T - \theta_p)$ where χ_M is the magnetic susceptibility, C is the Curie constant, T is the absolute temperature and θ_p is the paramagnetic Curie-Weiss temperature. Pr, Nd, Gd and Tb compounds obey the Curie-Weiss law over a wide temperature range while the Ce compound shows a strong deviation below 125K (Insets of Figures S7- S11). This phenomenon has been reported for other Ce^{3+} compounds and has been attributed to crystal field splitting of the $^2F_{5/2}$ ground state^{34, 35}. Note that the $Cs_2Ce_3CuS_8$ curve profile is similar to the one observed for $CsCe_2CuS_6$ and $CsCeCuS_3$ ¹¹. Results of Ce, Pr, Nd, Gd and Tb inverse susceptibility fits are summarized in Table 5. The obtained effective magnetic moment μ_{eff} are 2.95(1) μ_B/Ce^{3+} , 3.93(4) μ_B/Pr^{3+} , 3.70(3) μ_B/Nd^{3+} , 7.41(1) μ_B/Gd^{3+} and 9.69(1) μ_B/Tb^{3+} . These experimental values are consistent with theoretical ones for $Cs_2Nd_3CuS_8$ and $Cs_2Tb_3CuS_8$, they are significantly different for others compounds suggesting the presence of uncharacterized paramagnetic impurities in the samples. For $Cs_2Ce_3CuS_8$, the higher value of μ_{eff} than that expected is associated with a large negative θ_p value. Such effective magnetic moment deviation and large negative θ_p value has been also observed in $CsCeCuS_3$. The authors reported that the nature of the Ce oxidation state remains unclear and that valence fluctuations might occur in the compound.¹¹ For each compound, fitting parameters indicate negative paramagnetic Curie-Weiss temperatures θ_p (Table 5) suggesting local antiferromagnetic interactions.

Table 5. Fitted paramagnetic Curie-Weiss temperatures θ_p and effective magnetic moments μ_{eff} of the $Cs_2Ln_3CuS_8$ series

Compound	θ_p (K)	μ_{eff} (μ_B/Ln^{3+})	μ_{eff} (μ_B/Ln^{3+})	$\Delta(\mu_{eff})(\%)$
		this study	theoretical	
$Cs_2Ce_3CuS_8$	-142.9(7)	2.95(1)	2.54	+16

$\text{Cs}_2\text{Pr}_3\text{CuS}_8$	-40.8(5)	3.93(4)	3.58	+10
$\text{Cs}_2\text{Nd}_3\text{CuS}_8$	-41.5(3)	3.70(3)	3.6	+2
$\text{Cs}_2\text{Eu}_3\text{CuS}_8$	-203.4(5)	4.77(3) per Eu	0 per Eu^{3+} 7.94 per Eu^{2+}	- -
$\text{Cs}_2\text{Gd}_3\text{CuS}_8$	-5.6(1)	7.41(1)	7.94	-7
$\text{Cs}_2\text{Tb}_3\text{CuS}_8$	-13.6(1)	9.69(1)	9.72	-0.3

The temperature dependent magnetic susceptibility of $\text{Cs}_2\text{Eu}_3\text{CuS}_8$ is shown in Figure 4A. Two anomalies are visible at about 3K and 17 K (Figure 4B) and can be related respectively to the presence of ferromagnetic Eu_3S_4 ($T_C = 3.1$ K³⁶) and EuS ($T_C = 16.6$ K³⁷) as secondary phases. This is supported by the magnetization data recorded at low temperature (Figure S13). Note that the weakness of impurities signal on PXRD data (Figure S3 in SI, only EuS is visible) suggests that they are both contained as traces in the sample. At high temperature ($T > 100\text{K}$), the $\text{Cs}_2\text{Eu}_3\text{CuS}_8$ compound follows the Curie-Weiss law as illustrated on the inset of Figure 4A. The fit resulted in an effective magnetic moment of 4.77(3) μ_B per Eu atom and a paramagnetic Curie-Weiss temperature of -203.4(5) K (Table 5). The negative θ_p value indicates predominant antiferromagnetic interactions and the effective magnetic moment μ_{eff} lies in between Eu^{2+} and Eu^{3+} expected values. On the one hand, Eu^{2+} has a large spin quantum number $S=7/2$ and an orbital angular momentum $L=0$ which leads to a theoretical effective magnetic moment of 7.94 μ_B . On the other hand, Eu^{3+} has a spin quantum number $S=3$ and an orbital angular momentum $L=3$ that cancel each other, thus giving theoretically no effective magnetic moment. However, because of the narrow energy separation between its ground state 7F_0 and the successive excited states, at high temperature, Eu^{3+} ions give rise to Van Vleck paramagnetism with a magnetic moment $\mu_{\text{eff}} = 3.4 \mu_B$ ³⁸. This means that both $\text{Eu}^{2+}/\text{Eu}^{3+}$ cations contribute to the effective magnetic moment deduced from our Curie-Weiss fit. Outcomes from this fit thus confirm the existence of both Eu^{2+} and Eu^{3+}

cations in the material, which is in agreement with the single crystal structural refinement that leads to the following composition: $\text{Cs}_2\text{Eu}_3\text{Cu}_{1.46}\text{S}_8$. However, from these magnetic measurements we cannot unambiguously conclude on the $\text{Eu}^{2+}:\text{Eu}^{3+}$ ratio because of the ferromagnetic impurities that contain both species.

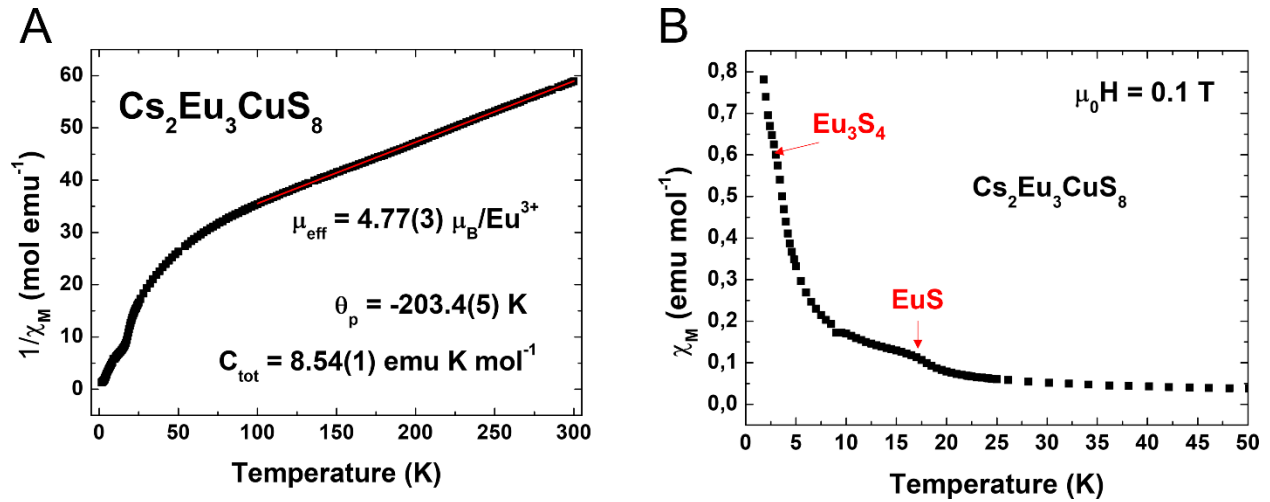


Figure 5. Temperature dependence of the molar magnetic susceptibility (χ_M) of $\text{Cs}_2\text{Eu}_3\text{CuS}_8$ recorded from 1.8 K to 300 K under an applied magnetic field of 0.1 T and of its inverse ($1/\chi_M$) fitted from 100 K to 300 K with the Curie-Weiss law (A). Zoom on the magnetic susceptibility of $\text{Cs}_2\text{Eu}_3\text{CuS}_8$ at low temperature (B).

Following our investigation on magnetocaloric properties of Gd sulfides,³⁹ those of the $\text{Cs}_2\text{Gd}_3\text{CuS}_8$ member were analyzed. Indeed, one can expect interesting magnetocaloric properties due to the large spin quantum number of Gd^{3+} ion ($S=7/2$) favoring a large magnetic entropy change. The magnetic entropy change determined from isothermal magnetization curves (Figure 5A) increases upon cooling down to 2.5 K for applied magnetic field changes of 1 and 2 T, and presents a maximum at 3.5 K for higher magnetic field variations (Figure 5B). $\text{Cs}_2\text{Gd}_3\text{CuS}_8$ is characterized by relatively large values of magnetic entropy change, reaching $6.7 \text{ J kg}^{-1} \text{ K}^{-1}$ (or $33 \text{ mJ cm}^{-3} \text{ K}^{-1}$) at 2.5 K for $\mu_0\Delta H = 2 \text{ T}$ and $19.5 \text{ J kg}^{-1} \text{ K}^{-1}$ (or $95 \text{ mJ cm}^{-3} \text{ K}^{-1}$) at 3.5 K for $\mu_0\Delta H =$

5 T. These values are comparable to those reported for Gd-based oxides⁴⁰⁻⁴² including the reference material $\text{Gd}_3\text{Ga}_5\text{O}_{12}$,⁴³ and superior, near liquid helium temperature, to those reported for Gd-based intermetallics⁴⁴⁻⁴⁷, borides⁴⁸, carbides,⁴⁹ and borocarbides.^{50,51} Nevertheless, the magnetocaloric effect of $\text{Cs}_2\text{Gd}_3\text{CuS}_8$ is significantly weaker than the one of NaGdS_2 .³⁹ This can be explained by the fact that, (i) $\text{Cs}_2\text{Gd}_3\text{CuS}_8$ suffers from a weak magnetic/non-magnetic mass ratio and (ii) the magnetization isotherms at low temperature are far from saturation even under an applied magnetic field of 5 T (Figure 5A), indicating non-negligible antiferromagnetic interactions between Gd centers. Moreover, the shape of the magnetization curve recorded at 2 K exhibits a metamagnetic-like transition that might be correlated to some kind of short-range magnetic ordering, thus supporting the existence of interactions between Gd^{3+} ions.

Magnetocaloric properties were also investigated for the other members of the $\text{Cs}_2\text{Ln}_3\text{CuS}_8$ family, but the effect is weaker, *i.e.* values of magnetic entropy change $< 1.5 \text{ J kg}^{-1} \text{ K}^{-1}$ excepted for the Tb compound where $-\Delta S_M$ reaches $8 \text{ J kg}^{-1} \text{ K}^{-1}$ at 5.5K. Results for the whole family are summarized in Table 6.

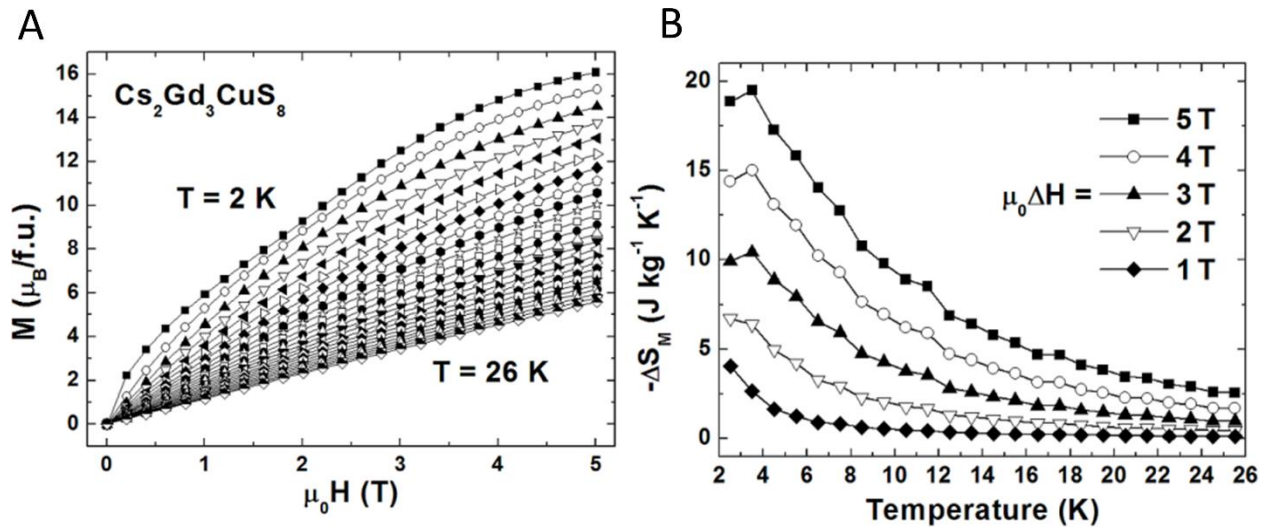


Figure 6. Magnetization isotherms of Cs₂Gd₃CuS₈ recorded from 2 K to 26 K in applied magnetic fields up to 5 T, with field steps of 0.2 T and temperature increments of 1 K (A). Temperature dependence of the mass magnetic entropy change ($-\Delta S_M$) in Cs₂Gd₃CuS₈ for field variation (B)

Table 6. Magnetocaloric properties of the Cs₂Ln₃CuS₈ series

Compound	T (K)	$-\Delta S_M$ (J kg ⁻¹ K ⁻¹)		$-\Delta S_M$ (mJ cm ⁻³ K ⁻¹)		ρ (g cm ⁻³)
		0-2 T	0-5 T	0-2 T	0-5 T	
Cs ₂ Ce ₃ CuS ₈	--	--	--	--	--	
Cs ₂ Pr ₃ CuS ₈	5	0.2	1.2	1.1	5.6	4.65
Cs ₂ Nd ₃ CuS ₈	3	0.2	0.8	0.8	3.4	4.51
Cs ₂ Eu ₃ CuS ₈	3	0.7	1.3	3.6	6.2	4.88
Cs ₂ Gd ₃ CuS ₈	3.5	6.4	19.5	31.1	95.1	4.88
Cs ₂ Tb ₃ CuS ₈	5.5	3.7	8	18.6	39.7	4.95

Theoretical considerations

DFT calculations were carried out for Cs₂La₃CuS₈. Since copper positions are half-occupied, several models had to be considered for the crystal structure of this compound. Assuming the unit-cell resulting from X-ray diffraction studies, three of them can be considered; they are sketched in Figure 7. Their crystal structures have lower symmetry than the parent compound. Assuming a chain of lanthanum atoms in the structure (...-La(1)-La(2)-La(1)-La(2)-...), their differences come from the position of Cu atoms with regard to this chain. In the *Bm* structure, only positions that lie on the same side of the chain are occupied. In the *P2/m* and *P2₁/m* structures, half of the positions located on each side of the chains are occupied. Optimized cell parameters and main bond distances are reported in Table 7. *P2/m* model is significantly energetically unfavored compared to the two other models. *P2₁/m* model is slightly more stable than the *Bm* model (+0.05 eV / unit cell). It is interesting to mention that the most stable model corresponds to the most compact unit cell.

Optimized bond distances are comparable for both models: Cu-S bond distances range from 2.27 to 2.45 Å, S-S bond distances range from 2.07 to 2.12 Å and La-S bond distances range from 2.72 to 3.02 Å.

The total and atom-projected DOS computed for the $P2_1/m$ model of $\text{Cs}_2\text{La}_3\text{CuS}_8$ is sketched in Figure 7. The valence band is mainly centered on sulfur and copper. The bottom of the conduction band is dominated by S levels and La f levels. A band gap of *ca* 2 eV is computed. This value is lower than the optical band gap. This difference partially originates from the underestimation of band gap computed with LDA et GGA exchange-correlation functional. Crystal Orbital Hamiltonian Population (COHP) were computed for different contacts in the structure; they represent a measure of the magnitude of the bonding as they correspond to the Hamiltonian population-weighted DOS. The conduction band exhibit antibonding bands for all Cu-S, S-S and La-S bonds in the structure, whereas the bottom of the valence band is bonding for the same bonds. The top of the valence band shows an antibonding S-S character; this is consistent with a single σ S-S bond as expected considering their distance close to 2.10 Å. It is noteworthy to mention that La-S bonds are optimized for hexacoordinated La atoms. This is not the case for octa-coordinated La atoms as shown by the corresponding COHP curves. The top of the valence band also exhibits an antibonding Cu-S character. This is often the case for Cu-S bonds in CuS_4 tetrahedron.

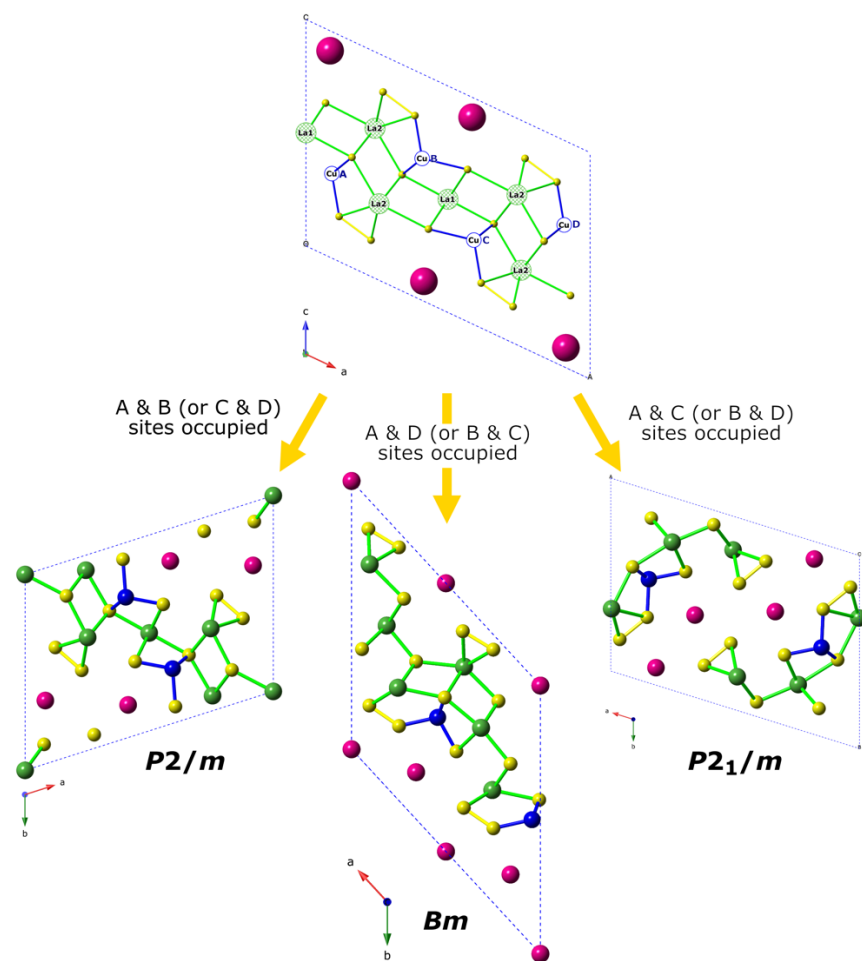


Figure 7. Different structural models considered for DFT calculations.

Table 7. Optimized cell parameters and selected bond lengths of used models

Models	$P2/m$	Bm	$P2_1/m$
Energy (eV /u.c.)	+0.24	+0.05	0
a (Å)	15.611	16.345	15.726
b (Å)	11.743	15.754	11.657
c (Å)	4.159	4.151	4.138
γ (°)	107.65	137.31	107.32
V (Å ³)	726.47	724.81	724.17

Cu-S (Å)	2.282, 2.286, 2.449 (x2)	2.283, 2.321, 2.416 (x2)	2.271, 2.304, 2.408 (x2)
S-S (Å)	2.087, 2.113	2.094, 2.116	2.076, 2.123
La-S (Å)	2.726 (x2), 2.824 (x4), 2.819 (x2), 2.828 (x2), 2.847 (x2), 2.794, 2.886 (x2), 2.886, 2.901 (x2), 2.926 (x2)	2.731, 2.776, 2.796 (x2), 2.882 (x2), 2.796 (x2), 2.811, 2.863 (x2), 3.060 (x2), 3.094, 2.832, 2.855, 2.872 (x2), 2.941 (x2), 2.981 (x2)	2.724, 2.815, 2.820 (x2), 2.855 (x2), 2.825 (x2), 2.851, 2.918 (x2), 2.944 (x2), 2.824 (x2), 2.828, 2.831, 2.944 (x2), 3.028 (x2)

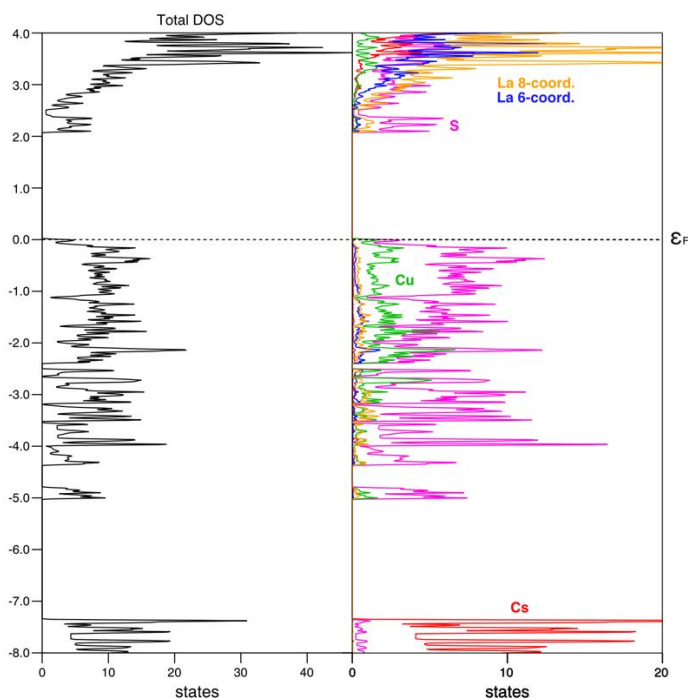


Figure 8. Total and atom-projected DOS computed for $\text{Cs}_2\text{La}_3\text{CuS}_8$ considering $\text{P2}_1/\text{m}$ model.

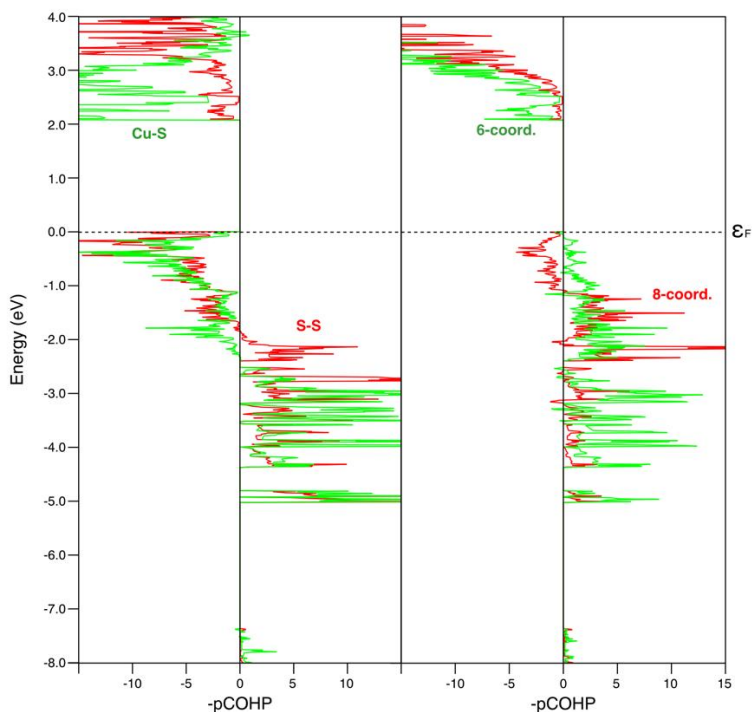


Figure 9. COHP computed for Cu-S contacts (ranging from 2.271 Å to 2.408 Å), S-S contacts (ranging from 2.076 Å to 2.123 Å) and La-S contacts (ranging from 2.724 Å to 3.028 Å) in $\text{Cs}_2\text{La}_3\text{CuS}_8$ considering $\text{P2}_1/\text{m}$ model.

Conclusions

In this work, we have demonstrated that the crystal structure of the new quaternary semiconducting sulfides $\text{Cs}_2\text{Ln}_3\text{CuS}_8$ is hybrid of those of ACe_2CuS_6 compounds ($\text{A} = \text{K}$ and Cs) and that of $\text{K}_2\text{Cu}_2\text{CeS}_4$ compound. The singularity of this structure is based on a complex framework built-up from two types of chains of rare earths generated by the two types of coordination polyhedrons of Ln^{3+} ions, the $\{\text{Ln}_2\text{S}_4(\text{S}_2)_2\}$ bicapped trigonal prisms and the $\{\text{Ln}_1\text{S}_6\}$ octahedrons, and their interconnections modes. It was found $\text{Cs}_2\text{Gd}_3\text{CuS}_8$ demonstrates a relatively large magnetocaloric effect near liquid helium temperature comparable with other effective Gd-based materials. This work highlights the route of lanthanide sulfides as a promising

magnetocaloric materials for magnetic refrigeration at cryogenic temperature either for gas liquefaction or ultra-low temperature applications.

AUTHOR INFORMATION

Corresponding Author

*naumov@niic.nsc.ru

Present Addresses

†Institut Jean Lamour, UMR 7198 CNRS, Université de Lorraine, 54011 Nancy, France

Author Contributions

The manuscript was written through contributions of all authors. All authors have given approval to the final version of the manuscript.

Supporting Information: Details of crystal structures for all compounds(selected bonds lengths, atomic parameters, anisotropic displacements parameters, additional figures of crystal structure), powder diffraction patterns of all compounds, optical absorption spectra of $\text{Cs}_2\text{Ln}_3\text{CuS}_8$ ($\text{Ln} = \text{Ce}, \text{Pr}, \text{Gd}, \text{Tb}$), temperature dependences of the molar magnetic susceptibility for $\text{Cs}_2\text{Ln}_3\text{CuS}_8$ ($\text{Ce}, \text{Pr}, \text{Gd}, \text{Tb}$) and magnetization isotherms of all the $\text{Cs}_2\text{Ln}_3\text{CuS}_8$ series.

Funding Sources

The research was supported by the Ministry of Science and Higher Education of the Russian Federation, N 121031700315-2.

REFERENCES

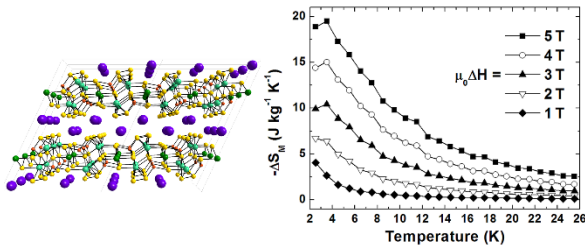
(1) Mitchell, K.; Huang, F. Q.; Caspi, E. a. N.; McFarland, A. D.; Haynes, C. L.; Somers, R. C.; Jorgensen, J. D.; Van Duyne, R. P.; Ibers, J. A. Syntheses, Structure, and Selected Physical

- Properties of CsLnMnSe₃ (Ln= Sm, Gd, Tb, Dy, Ho, Er, Tm, Yb, Y) and AYbZnQ₃ (A= Rb, Cs; Q= S, Se, Te). *Inorg. Chem.* **2004**, *43* (3), 1082-1089.
- (2) Mitchell, K.; Huang, F. Q.; McFarland, A. D.; Haynes, C. L.; Somers, R. C.; Van Duyne, R. P.; Ibers, J. A. The CsLnMSe₃ Semiconductors (Ln= Rare-Earth Element, Y; M= Zn, Cd, Hg). *Inorg. Chem.* **2003**, *42* (13), 4109-4116.
- (3) Meng, C.-Y.; Chen, H.; Wang, P.; Chen, L. Syntheses, Structures, and Magnetic and Thermoelectric Properties of Double-Tunnel Tellurides: A_xRE₂Cu_{6-x}Te₆ (A= K–Cs; RE= La–Nd). *Chem. Mater.* **2011**, *23* (22), 4910-4919.
- (4) Zhao, H.-J.; Zhang, Y.-F.; Chen, L. Strong Kleinman-forbidden second harmonic generation in chiral sulfide: La₄InSbS₉. *J. Am. Chem. Soc.* **2012**, *134* (4), 1993-1995.
- (5) Zhao, H. J. Synthesis, crystal structure, and NLO property of the chiral sulfide Sm₄InSbS₉. *Z. Anorg. Allg. Chem.* **2016**, *642* (1), 56-59.
- (6) Malliakas, C. D.; Kanatzidis, M. G. Charge Density Waves in the Square Nets of Tellurium of AMRETe₄ (A= K, Na; M= Cu, Ag; RE= La, Ce). *J. Am. Chem. Soc.* **2007**, *129* (35), 10675-10677.
- (7) Kanatzidis, M. G. Discovery-synthesis, design, and prediction of chalcogenide phases. *Inorg. Chem.* **2017**, *56* (6), 3158-3173.
- (8) Mitchell, K.; Ibers, J. A. Rare-earth transition-metal chalcogenides. *Chem. Rev.* **2002**, *102* (6), 1929-1952.
- (9) Yao, J.; Deng, B.; Ellis, D. E.; Ibers, J. A. Syntheses, structures, physical properties, and electronic structures of KLn₂CuS₄ (Ln= Y, Nd, Sm, Tb, Ho) and K₂Ln₄Cu₄S₉ (Ln= Dy, Ho). *J. Solid State Chem.* **2003**, *176* (1), 5-12.
- (10) Sutorik, A. C.; Albritton-Thomas, J.; Kannewurf, C. R.; Kanatzidis, M. G. The First Examples of Alkali Metal/Cu/Ce/Chalcogenides: The Layered Heterometallic Compounds KCuCe₂S₆ and K₂Cu₂CeS₄. *J. Am. Chem. Soc.* **1994**, *116* (17), 7706-7713.
- (11) Sutorik, A. C.; Albritton-Thomas, J.; Hogan, T.; Kannewurf, C. R.; Kanatzidis, M. G. New quaternary compounds resulting from the reaction of copper and *f*-block metals in molten polychalcogenide salts at intermediate temperatures. Valence fluctuations in the layered CsCuCeS₃. *Chem. Mater.* **1996**, *8* (3), 751-761.
- (12) Bensch, W.; Dürichen, P. Preparation and Crystal Structure of the New Quaternary Europium-polysulfide KCuEu₂S₆. *Chem. Ber.* **1996**, *129* (12), 1489-1492.
- (13) Pomelova, T. A.; Podlipskaya, T. Y.; Kuratieva, N. V.; Cherkov, A. G.; Nebogatikova, N. A.; Ryzhikov, M. R.; Huguenot, A.; Gautier, R. g.; Naumov, N. G. Synthesis, Crystal Structure, and Liquid Exfoliation of Layered Lanthanide Sulfides KLn₂CuS₆ (Ln= La, Ce, Pr, Nd, Sm). *Inorg. Chem.* **2018**, *57* (21), 13594-13605.
- (14) Lauxmann, P.; Schleid, T. CsCu₃Dy₂S₅ und CsCu₃Er₂S₅: Zwei isotype quaternäre Sulfide der Lanthanoide mit Kanalstrukturen/CsCu₃Dy₂S₅ und CsCu₃Er₂S₅: Two Isotypic Quaternary Sulfides of the Lanthanides with Channel Structures. *Z. Naturforsch. B* **2001**, *56* (11), 1149-1154.
- (15) Huang, F. Q.; Ibers, J. A. Syntheses, structures, and physical properties of the new quaternary rare-earth chalcogenides RbNd₂CuS₄, RbSm₂CuS₄, CsLa₂CuSe₄, CsSm₂CuSe₄, RbEr₂Cu₃S₅, CsGd₂Ag₃Se₅, CsTb₂Ag₃Se₅, and Rb₂Gd₄Cu₄S₉. *J. Solid State Chem.* **2001**, *158* (2), 299-306.
- (16) Toby, B. H.; Von Dreele, R. B. GSAS-II: the genesis of a modern open-source all purpose crystallography software package. *J. Appl. Crystallogr.* **2013**, *46* (2), 544-549.

- (17) Bruker, A. SAINT (Version 8.18 c), and SADABS (Version 2.11). *Bruker Advanced X-ray Solutions, Bruker AXS Inc., Madison, WI, USA* **2000**, 2012.
- (18) Sheldrick, G. M. Crystal structure refinement with SHELXL. *Acta Crystallogr., Sect. C: Cryst. Struct. Commun.*, **2015**, 71 (1), 3-8.
- (19) Bain, G. A.; Berry, J. F. Diamagnetic corrections and Pascal's constants. *J. Chem. Educ.* **2008**, 85 (4), 532.
- (20) Pecharsky, V.; Gschneidner Jr, K. Magnetocaloric effect from indirect measurements: Magnetization and heat capacity. *J. Appl. Phys.* **1999**, 86 (1), 565-575.
- (21) Kresse, G.; Furthmüller, J. Efficient iterative schemes for ab initio total-energy calculations using a plane-wave basis set. *Phys. Rev. B* **1996**, 54 (16), 11169.
- (22) Perdew, J. P.; Burke, K.; Ernzerhof, M. Generalized gradient approximation made simple. *Phys. Rev. Lett.* **1996**, 77 (18), 3865.
- (23) Monkhorst, H. J.; Pack, J. D. Special points for Brillouin-zone integrations. *Phys. Rev. B* **1976**, 13 (12), 5188.
- (24) Dronskowski, R.; Blochl, P. E. Crystal orbital Hamilton populations (COHP): energy-resolved visualization of chemical bonding in solids based on density-functional calculations. *J. Phys. Chem.* **1993**, 97 (33), 8617-8624.
- (25) Deringer, V. L.; Tchougréeff, A. L.; Dronskowski, R. Crystal orbital Hamilton population (COHP) analysis as projected from plane-wave basis sets. *J. Phys. Chem. A*, **2011**, 115 (21), 5461-5466.
- (26) Maintz, S.; Deringer, V. L.; Tchougréeff, A. L.; Dronskowski, R. Analytic projection from plane-wave and PAW wavefunctions and application to chemical-bonding analysis in solids. *J. Comput. Chem.* **2013**, 34 (29), 2557-2567.
- (27) Maintz, S.; Deringer, V. L.; Tchougréeff, A. L.; Dronskowski, R. LOBSTER: A tool to extract chemical bonding from plane-wave based DFT. Wiley Online Library: 2016.
- (28) Will, G.; Lauterjung, J.; Schmitz, H.; Hinze, E. The bulk moduli of 3d-transition element pyrites measured with synchrotron radiation in a new belt type apparatus. In *Materials Research Society symposium proceedings: MRSSP*, 1984; Vol. 22, pp 49-52.
- (29) Morris, C. D.; Li, H.; Jin, H.; Malliakas, C. D.; Peters, J. A.; Trikalitis, P. N.; Freeman, A. J.; Wessels, B. W.; Kanatzidis, M. G. Cs₂M^{II}M^{IV}₃Q₈ (Q= S, Se, Te): an extensive family of layered semiconductors with diverse band gaps. *Chem. Mater.* **2013**, 25 (16), 3344-3356.
- (30) Palchik, O.; Marking, G. M.; Kanatzidis, M. G. Exploratory synthesis in molten salts: Role of flux basicity in the stabilization of the complex thiogermanates Cs₄Pb₄Ge₅S₁₆, K₂PbGe₂S₆, and K₄Sn₃Ge₃S₁₄. *Inorg. Chem.* **2005**, 44 (12), 4151-4153.
- (31) Pogu, A.; Vidyasagar, K. Syntheses, structural variants and characterization of A₂ZnSn₃S₈ (A= Cs, Rb) and A₂CdSn₃S₈ (A= Cs, Rb, K, Na) compounds. *J. Solid State Chem.* **2020**, 291, 121647.
- (32) Luo, X.; Liang, F.; Zhou, M.; Guo, Y.; Li, Z.; Lin, Z.; Yao, J.; Wu, Y. K₂ZnGe₃S₈: a congruent-melting infrared nonlinear-optical material with a large band gap. *Inorg. Chem.* **2018**, 57 (15), 9446-9452.
- (33) Choudhury, A.; Dorhout, P. K. Synthesis, Structure, Magnetic and Optical Properties of Ternary Thio-germanates: Ln₄(GeS₄)₃ (Ln= Ce, Nd). *Z. Anorg. Allg. Chem.* **2008**, 634 (4), 649-656.
- (34) Lueken, H.; Brüggemann, W.; Bronger, W.; Fleischhauer, J. Magnetic properties of NaCeS₂ between 3.7 and 297 K. *J. less-common met.* **1979**, 65 (1), 79-88.

- (35) Duczmal, M.; Pawlak, L. The crystal field influence on magnetic susceptibilities of TlCeSe₂ and TlCeTe₂. *J. Magn. Magn. Mater.* **1988**, *76*, 195-196.
- (36) Massenet, O.; Coey, J.; Holtzberg, F. Phase transition and magnetism in Eu₃S₄. *Le Journal de Physique Colloques* **1976**, *37* (C4), C4-297-C294-299.
- (37) Mauger, A.; Godart, C. The magnetic, optical, and transport properties of representatives of a class of magnetic semiconductors: The europium chalcogenides. *Phys. Rep.* **1986**, *141* (2-3), 51-176.
- (38) Takikawa, Y.; Ebisu, S.; Nagata, S. Van Vleck paramagnetism of the trivalent Eu ions. *J. Phys. Chem. Solids*, **2010**, *71* (11), 1592-1598.
- (39) Delacotte, C. n.; Pomelova, T. A.; Stephant, T.; Guizouarn, T.; Cordier, S.; Naumov, N. G.; Lemoine, P. NaGdS₂: A Promising Sulfide for Cryogenic Magnetic Cooling. *Chem. Mater.* **2022**.
- (40) Dong, Z.; Yin, S. Structural, magnetic and magnetocaloric properties in perovskite RE₂FeCoO₆ (RE= Er and Gd) compounds. *Ceram. Int.* **2020**, *46* (1), 1099-1103.
- (41) Palacios, E.; Tomasi, C.; Sáez-Puche, R.; Dos santos-García, A.; Fernández-Martínez, F.; Burriel, R. Effect of Gd polarization on the large magnetocaloric effect of GdCrO₄ in a broad temperature range. *Phys. Rev. B* **2016**, *93* (6), 064420.
- (42) Dey, K.; Indra, A.; Majumdar, S.; Giri, S. Cryogenic magnetocaloric effect in zircon-type RVO₄ (R= Gd, Ho, Er, and Yb). *J. Mater. Chem. C* **2017**, *5* (7), 1646-1650.
- (43) Hamilton, A. S.; Lampronti, G.; Rowley, S.; Dutton, S. Enhancement of the magnetocaloric effect driven by changes in the crystal structure of Al-doped GGG, Gd₃Ga_{5-x}Al_xO₁₂ (0 ≤ x ≤ 5). *J. Phys. Condens. Matter.* **2014**, *26* (11), 116001.
- (44) Rawat, R.; Das, I. Heat capacity and magnetocaloric studies of RPd₂Si (R= Gd, Tb and Dy). *J. Phys. Condens. Matter.* **2006**, *18* (3), 1051.
- (45) Pakhira, S.; Mazumdar, C.; Ranganathan, R.; Giri, S.; Avdeev, M. Large magnetic cooling power involving frustrated antiferromagnetic spin-glass state in R₂NiSi₃ (R= Gd, Er). *Phys. Rev. B* **2016**, *94* (10), 104414.
- (46) Pakhira, S.; Mazumdar, C.; Ranganathan, R. Magnetic and magnetocaloric properties of (Gd_{1-x}Y_x)₂NiSi₃ compounds (x= 0.25, 0.5, 0.75). *J. Magn. Magn. Mater.* **2019**, *484*, 456-461.
- (47) Pani, M.; Morozkin, A.; Yapaskurt, V.; Provino, A.; Manfrinetti, P.; Nirmala, R.; Malik, S. RNi₈Si₃ (R= Gd, Tb): Novel ternary ordered derivatives of the BaCd11 type. *J. Solid State Chem.* **2016**, *233*, 397-406.
- (48) Li, L.; Nishimura, K.; Yamane, H. Giant reversible magnetocaloric effect in antiferromagnetic GdCo₂B₂ compound. *Appl. Phys. Lett.* **2009**, *94* (10), 102509.
- (49) Meng, L.; Xu, C.; Yuan, Y.; Qi, Y.; Zhou, S.; Li, L. Magnetic properties and giant reversible magnetocaloric effect in GdCo₂. *RSC Adv.* **2016**, *6* (78), 74765-74768.
- (50) Zhang, Y.; Guo, D.; Wu, B.; Wang, H.; Guan, R.; Li, X.; Ren, Z. Magnetic properties and magneto-caloric performances in RECo₂B₂C (RE= Gd, Tb and Dy) compounds. *J. Alloys Compd.* **2020**, *817*, 152780.
- (51) Li, L.; Kadonaga, M.; Huo, D.; Qian, Z.; Namiki, T.; Nishimura, K. Low field giant magnetocaloric effect in RNiBC (R= Er and Gd) and enhanced refrigerant capacity in its composite materials. *Appl. Phys. Lett.* **2012**, *101* (12), 122401.

Table of Content



Novel compounds $\text{Cs}_2\text{Ln}_3\text{CuS}_8$ ($\text{Ln}=\text{La-Nd,Sm-Tb}$) has been prepared by reactive flux method from mixture of component sulfides. These compounds have layered-like structure lies between $\text{CsCe}_2\text{CuS}_6$ and K_2CeCuS_4 structural types. Optical band gaps of the compounds decrease with Ln radii increasing from 2.62 eV for Tb compound to 2.29 for La one with exceptions for $\text{Ln}=\text{Ce, Eu}$ which band gap is lower. Magnetic measurements reveal that the $\text{Cs}_2\text{Gd}_3\text{CuS}_8$ displayed considerable magnetocaloric effect near liquid helium temperature.